PCCP

PAPER

View Article Online
View Journal | View Issue

Cite this: *Phys. Chem. Chem. Phys.*, 2025, **27**, 218

Doped hexa-*peri*-hexabenzocoronene as anode materials for lithium- and magnesium-ion batteries†

Remya Geetha Sadasivan Nair,* Arun Kumar Narayanan Nair,* Bicheng Yan* and Shuyu Sun*

Received 25th October 2024,
Accepted 25th November 2024

DOI: 10.1039/d4cp04101a

rsc.li/pccp

The adsorption processes of Li^+, Li, Mg^{2+}, and Mg on twelve adsorbents (pristine and N/BN/Si-doped hexa-*peri*-hexabenzocoronene (HBC) molecules) were studied using density functional theory. The molecular electrostatic potential (MESP) analyses show that the replacement of C atoms of HBC by N/BN/Si units can provide a more electron-rich system than the parent HBC molecule. Li^+ and Mg^{2+} exhibit strong adsorption on pristine and doped HBC molecules. The adsorption energy of cations on these nanoflakes ($E_{ads\text{-}1}$) was in the range of −247.44 (Mg^{2+}/*m*-$C_{40}H_{18}N_2$ system) to −47.65 kcal mol^{-1} ($Li^+/B_{21}H_{18}N_{21}$ system). Importantly, our results suggest the weaker interactions of Li^+ and Mg^{2+} with the nanoflakes as the MESP minimum values of the nanoflakes became less negative. In all studied systems, we observed electron donation from the nanoflakes to Li^+ and Mg^{2+}. For the metal/nanoflake systems, the adsorption energy of metals on the nanoflakes ($E_{ads\text{-}2}$) was in the range of −33.94 ($Li/C_{38}H_{18}B_2N_2$ system) to −2.14 kcal mol^{-1} ($Mg/B_{21}H_{18}N_{21}$ system). Among the studied anode materials for lithium-ion batteries (LIBs), the highest cell voltage (V_{cell}) of 1.90 V was obtained for $B_{21}H_{18}N_{21}$. Among the studied anode materials for magnesium-ion batteries (MIBs), the highest V_{cell} value of 5.29 V was obtained for *m*-$C_{40}H_{18}N_2$. $E_{ads\text{-}2}$ has a significant effect on the variation of V_{cell} of LIBs, while $E_{ads\text{-}1}$ has a significant effect on the variation of V_{cell} of MIBs.

1. Introduction

Rechargeable energy storage devices like lithium-ion batteries (LIBs) are in high demand due to their potential applications in electronic devices and electric transportation.[1–3] Since the commercialization by Sony Corporation in 1991,[1–3] LIBs have dominated the markets of portable electronic devices and electric vehicles because of their high energy densities and long cycle lives. LIBs are mainly composed of an anode, a cathode, and an electrolyte. Lithium cobalt oxide, lithium iron phosphate, and lithium manganese oxide are typically used as cathode materials for LIBs. The electrolyte of LIBs is mostly based on a lithium salt dissolved in organic solvents. Carbon materials like graphene, carbon nanofibers, carbon nanotubes, polycyclic aromatic hydrocarbons (PAHs), *etc.* have been frequently employed for the construction of anode materials for LIBs.[4–9] For instance, the high surface areas, electrical conductivities, and mechanical flexibilities of graphene make it a good candidate for anode materials in LIBs.[5] Park *et al.* achieved good rate capabilities and cycling stability for LIBs by employing PAH in the design of anode materials.[7] Arya *et al.* also obtained good cycling stability, high specific capacity, and excellent rate capability for LIBs by employing PAHs in the design of anode materials.[9] Doped carbon materials have also been employed for the construction of anode materials for LIBs.[10–13] Recently, divalent metal-ion batteries such as magnesium-ion batteries (MIBs) have attracted considerable interest.[14,15] Mg could donate two valence electrons and therefore higher storage capacities may be realized in MIBs than in LIBs. Additional features of MIBs such as natural abundance of Mg, lower costs, and good safety make them an excellent alternative to LIBs.[16]

PAHs consist of multiple aromatic rings and are rich in delocalized π-electrons. Planar PAHs like coronene, hexa-*peri*-hexabenzocoronene (HBC), and circumcoronene are formed by fusion of 7, 13, and 19 benzene rings, respectively. These planar PAHs may be considered as finite-size models of graphene. Great progress has been made in the design and synthesis of different heteroatom-doped PAHs.[17–20] For example, the synthesis of HBC with a central borazine core was reported by

Physical Science and Engineering Division (PSE), King Abdullah University of Science and Technology (KAUST), Thuwal 23955-6900, Saudi Arabia.
E-mail: remya.nair@kaust.edu.sa, arun.narayanannair@kaust.edu.sa, bicheng.yan@kaust.edu.sa, shuyu.sun@kaust.edu.sa

† Electronic supplementary information (ESI) available: Additional details of DFT analysis. See DOI: https://doi.org/10.1039/d4cp04101a

Krieg *et al.* in 2015.[17] There have been several studies of molecular adsorption on pristine and doped PAHs using density functional theory (DFT).[21,22] There have also been studies of the application of pristine and doped PAHs as anode materials in metal-ion batteries using DFT.[23–29] Li^+ and Li were observed to be bound to the peripheral benzene rings of coronene and circumcoronene.[23] On the basis of cell voltage (V_{cell}), PAHs such as circumbiphenyl and coronene were recommended as good anode materials for LIBs.[24] Li has a higher interaction with circumcoronene than with BN-circumcoronene.[23] Li^+ and Li were found to be bound to the peripheral rings of HBC.[25] Li^+ and Li were also bound to the peripheral rings of BN-doped HBC.[26] Mg^{2+} was chemically adsorbed on HBC, while Mg was physically adsorbed on HBC.[27] For the sodium-ion batteries, the V_{cell} value obtained using HBC with a central borazine core was lower than that obtained using the pristine HBC.[28] A similar result was obtained for the calcium-ion batteries.[29] However, the interactions of Mg^{2+} and Mg with adsorbents like Si-doped HBC have not yet been investigated.

In the present study, DFT calculations were carried out to understand the adsorption process of Li^+, Li, Mg^{2+}, and Mg on twelve nanoflakes (pristine and N/BN/Si-doped HBC molecules). The molecular electrostatic potential (MESP) minimum point (designated as V_{min}) is often observed at the electron-rich sites like lone pairs and π-regions.[30–32] Importantly, our results suggest the weaker interactions of Li^+ and Mg^{2+} with the nanoflakes as the MESP V_{min} values of the nanoflakes become less negative. For LIBs, the highest V_{cell} value of 1.90 V was obtained for $B_{21}H_{18}N_{21}$ and for MIBs, the highest V_{cell} value of 5.29 V was obtained for *m*-$C_{40}H_{18}N_2$. This study can provide some new insights into the design and exploration of anode materials suitable for metal ion batteries.

2. Computational details

All DFT computations were conducted through the Gaussian 16 program.[33] In the present study, we use a total of twelve adsorbents (pristine and N/BN/Si-doped HBC molecules $C_{42}H_{18}$, *o*-$C_{40}H_{18}N_2$, *m*-$C_{40}H_{18}N_2$, *p*-$C_{40}H_{18}N_2$, *o*-$C_{40}H_{18}BN$, *m*-$C_{40}H_{18}BN$, *p*-$C_{40}H_{18}BN$, $C_{38}H_{18}B_2N_2$, $C_{36}H_{18}B_3N_3$, $C_{28}H_{18}Si_{14}$, $C_{21}H_{18}Si_{21}$, and $B_{21}H_{18}N_{21}$) and four adsorbates (Li^+, Li, Mg^{2+}, and Mg). The adsorbents were obtained by the replacement of C atoms of HBC by N/BN/Si units. The structural isomers of, for instance, $C_{40}H_{18}N_2$ (two nitrogen atoms occupied adjacent positions in *o*-$C_{40}H_{18}N_2$) were considered in this work. Note that, $C_{28}H_{18}Si_{14}$, $C_{21}H_{18}Si_{21}$, and $B_{21}H_{18}N_{21}$ may be considered as finite-size models of graphene-like SiC_2, SiC, and BN nanosheets, respectively. All structures are optimized at the M062X/6-31G(d,p) level[34] and characterized as energy minima by frequency calculations. M06-2X is a hybrid meta functional with 54% of exact Hartree–Fock (HF) exchange. It is a high-nonlocality functional with double the amount of nonlocal exchange (2X) and it also considers the dispersion forces. The M06-2X functional is parameterized for nonmetals and recommended for the study of noncovalent interactions, kinetics, and main-group thermochemistry. The 6-31G(d,p) basis set was used for the geometry optimization calculations. In the geometry optimization process, the geometry is adjusted until a stationary point on the potential surface is found. Vibrational frequency analysis has been carried out to ensure that all the optimized structures correspond to the local minima containing only positive vibrational frequencies.

MESP $V(r)$[30–32] is described by the following expression:

$$V(\mathbf{r}) = \sum_{A=1}^{N} \frac{Z_A}{|\mathbf{r} - \mathbf{R}_A|} - \int \frac{\rho(\mathbf{r}')}{|\mathbf{r} - \mathbf{r}'|} \mathrm{d}^3\mathbf{r}' \quad (1)$$

where Z_A denotes the charge on nucleus A positioned at $\mathbf{R}_A$ and $\rho(\mathbf{r})$ denotes the electron density. The first and second terms in eqn (1) represent the nuclear and electronic contributions to the MESP, respectively. $V(\mathbf{r})$ is positive when the first term in eqn (1) dominates and negative when the second term dominates. The MESP analysis was performed at the M062X/6-31G(d,p) level of theory.

The adsorption energy (E_{ads}) is described by the following expression:

$$E_{ads} = E_{adsorbate/nanoflake} - (E_{nanoflake} + E_{adsorbate}) + E_{BSSE} \quad (2)$$

where $E_{adsorbate/nanoflake}$, $E_{nanoflake}$, and $E_{adsorbate}$ denote the energies of the adsorbed system, adsorbent (*e.g.*, HBC), and adsorbate (Li^+/Li/Mg^{2+}/Mg), respectively. E_{BSSE} denotes the basis set superposition error energy calculated using the counterpoise approach.[35] The E_{ads} of Li^+/Mg^{2+} and Li/Mg on the nanoflakes was denoted as $E_{ads\text{-}1}$ and $E_{ads\text{-}2}$, respectively. The adsorption energies calculated in our study are in line with previous DFT data[25–27] (Fig. 1 and Table S1, ESI†). The adsorption free energy (G_{ads}) is described by the following expression:

$$G_{ads} = G_{adsorbate/nanoflake} - (G_{nanoflake} + G_{adsorbate}) \quad (3)$$

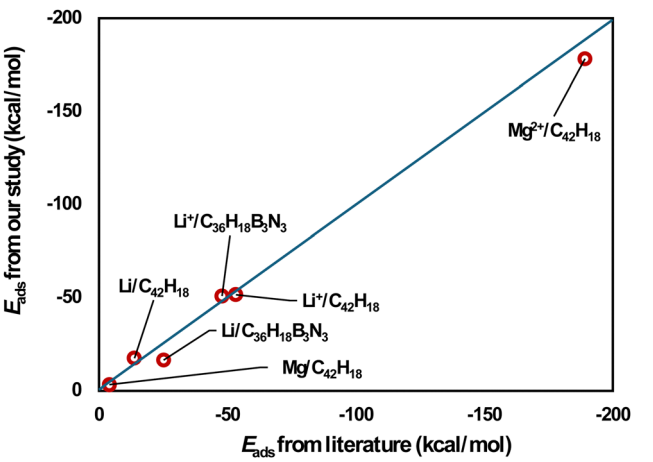

Fig. 1 Comparison of our results for adsorption energies with literature values.[25–27]

where $G_{adsorbate/nanoflake}$, $G_{adsorbate}$, and $G_{nanoflake}$ denote the free energies of the adsorbed system, adsorbent, and adsorbate, respectively.

The highest occupied molecular orbital (HOMO)–lowest unoccupied molecular orbital (LUMO) energy gap (E_g) can be calculated using the below equation:

$$E_g = E_{LUMO} - E_{HOMO} \quad (4)$$

where E_{HOMO} and E_{LUMO} denote the HOMO and LUMO energies, respectively. The E_g of the pristine nanoflake, the Li^+/Mg^{2+}-adsorbed nanoflake, and the Li/Mg-adsorbed nanoflake is denoted by $E_{g\text{-}1}$, $E_{g\text{-}2}$, and $E_{g\text{-}3}$, respectively.

The percentage change in the HOMO–LUMO energy gap can be calculated using the below equations:

$$\Delta E_{g\text{-}1} = [(E_{g\text{-}2} - E_{g\text{-}1})/E_{g\text{-}1}] \times 100 \quad (5)$$

$$\Delta E_{g\text{-}2} = [(E_{g\text{-}3} - E_{g\text{-}1})/E_{g\text{-}1}] \times 100 \quad (6)$$

For using a nanoflake as an anode material in, for example, MIBs, the reactions in the anode and cathode can be written as:

$$\text{Anode: Mg/nanoflake} \leftrightarrow Mg^{2+}\text{/nanoflake} + 2e^- \quad (7)$$

$$\text{Cathode: } Mg^{2+} + 2e^- \leftrightarrow Mg \quad (8)$$

Therefore, the total cell reaction is:

$$\text{Mg/nanoflake} + Mg^{2+} \leftrightarrow Mg^{2+}\text{/nanoflake} + Mg + \Delta G_{cell} \quad (9)$$

The Gibbs free energy change for the total cell reaction (ΔG_{cell}) is described by the following expression:

$$\Delta G_{cell} = \Delta E_{cell} + P\Delta V - T\Delta S \quad (10)$$

where

$$\Delta E_{cell} = E_{ads\text{-}1} - E_{ads\text{-}2} \quad (11)$$

The cell voltage can be calculated using the Nernst equation:

$$V_{cell} = -\Delta G_{cell}/zF \quad (12)$$

where F is the Faraday constant (96485.3 C mol^{-1}) and z is the valence of Li^+/Mg^{2+}. It might be assumed that $\Delta G_{cell} \approx \Delta E_{cell}$, because the contributions of the entropy effect and the volume effect to V_{cell} are expected to be negligible.[36]

3. Results and discussion

3.1 Doped HBC molecules as anode materials in lithium-ion batteries

3.1.1. Structural properties of doped HBC molecules. Fig. 2 provides the optimized configurations and the relevant bond lengths for the pristine and doped HBC molecules. The XY (X = C, B; Y = C, N, Si) bond lengths in the pristine and doped HBC molecules span from 1.36 to 1.83 Å. The carbon–carbon bond lengths in HBC span from 1.38 to 1.46 Å. This result is in good agreement with the experimental data.[37] Clar's aromatic sextet rule can be applied for HBC[38] and thus the carbon–carbon bond length in the central and the six peripheral benzene rings of HBC spans from 1.38 to 1.42 Å. For comparison, the carbon–carbon bond length in benzene is about 1.395 Å.[39] In all cases, the carbon–silicon bond lengths (>1.76 Å) are significantly longer than the carbon–carbon bond lengths.

Table 1 lists the E_{HOMO}, E_{LUMO}, and $E_{g\text{-}1}$ values of the pristine and doped HBC molecules. Here the E_{HOMO}, E_{LUMO}, and $E_{g\text{-}1}$ values are in the ranges of −8.10 ($B_{21}H_{18}N_{21}$) to −4.01 eV (m-$C_{40}H_{18}N_2$), −1.74 ($C_{38}H_{18}B_2N_2$) to 0.89 eV ($B_{21}H_{18}N_{21}$), and 2.46 (m-$C_{40}H_{18}N_2$) to 9.00 eV ($B_{21}H_{18}N_{21}$), respectively. The E_{HOMO}, E_{LUMO}, and $E_{g\text{-}1}$ values of HBC are −6.39, −1.00, and 5.40 eV, respectively. These results are in good agreement with previous theoretical calculations.[40] Overall, the E_{HOMO} (E_{LUMO}) values of the doped HBC molecules are higher (lower) than those of the pristine HBC. Also, in general, the $E_{g\text{-}1}$ values of the doped HBC molecules are lower than those of the pristine HBC. A smaller $E_{g\text{-}1}$ value usually indicates a higher electronic conductivity. However, the $E_{g\text{-}1}$ values of $C_{36}H_{18}B_3N_3$ and $B_{21}H_{18}N_{21}$ are higher than those of the pristine HBC.

3.1.2. MESP of doped HBC molecules. Fig. 3 displays the MESP surfaces of the pristine and doped HBC molecules. The MESP plots show the electron-rich region (*e.g.*, green region) on the central and peripheral benzene rings of HBC arising from the cyclic delocalization of π-electrons. Our results show that the replacement of C atoms of HBC by N/BN/Si units can provide a more electron-rich environment (*e.g.*, the blue region). Fig. S1, ESI,† provides the location of the MESP V_{min} of the pristine and doped HBC molecules. The MESP V_{min} points were situated near the six peripheral benzene rings of HBC. This indicates the higher electron-richness of the peripheral benzene rings of HBC as compared to the inner rings of HBC. This is due to the fact that the peripheral benzene rings of HBC also have carbon–hydrogen bonds and hydrogen is less electronegative than the sp^2 carbon. Overall, the MESP V_{min} points of all doped HBC molecules were also situated near the peripheral rings. However, the MESP V_{min} points of o-$C_{40}H_{18}N_2$ are situated near the inner N atoms. The MESP V_{min} values of the pristine and doped HBC molecules are listed in Table 1. A higher negative value of MESP V_{min} reflects a more electron rich nature of the nanoflake. These values were in the range of −31.38 ($C_{28}H_{18}Si_{14}$) to −15.56 kcal mol^{-1} ($C_{42}H_{18}$). A higher negative value of MESP V_{min} reflects a more electron rich nature of the nanoflake. The MESP V_{min} value of the doped HBC molecules was more negative than that of the pristine HBC. In the case of N-doped HBC molecules, the absolute value of MESP V_{min} followed the order p-$C_{40}H_{18}N_2$ < o-$C_{40}H_{18}N_2$ < m-$C_{40}H_{18}N_2$. In the case of BN-doped HBC molecules, the absolute value of MESP V_{min} followed the order $C_{36}H_{18}B_3N_3$ < $B_{21}H_{18}N_{21}$ < $C_{38}H_{18}B_2N_2$ < o-$C_{40}H_{18}BN$ < p-$C_{40}H_{18}BN$ < m-$C_{40}H_{18}BN$. The MESP V_{min} value of $C_{21}H_{18}Si_{21}$ (−28.43 kcal mol^{-1}) was less negative than that of $C_{28}H_{18}Si_{14}$ (−31.38 kcal mol^{-1}).

3.1.3. Li^+ adsorption on doped HBC molecules. Fig. 4 provides the optimized configurations and the adsorption distances for the adsorption of Li^+ on pristine and doped HBC molecules. We see that Li^+ is bound to the peripheral

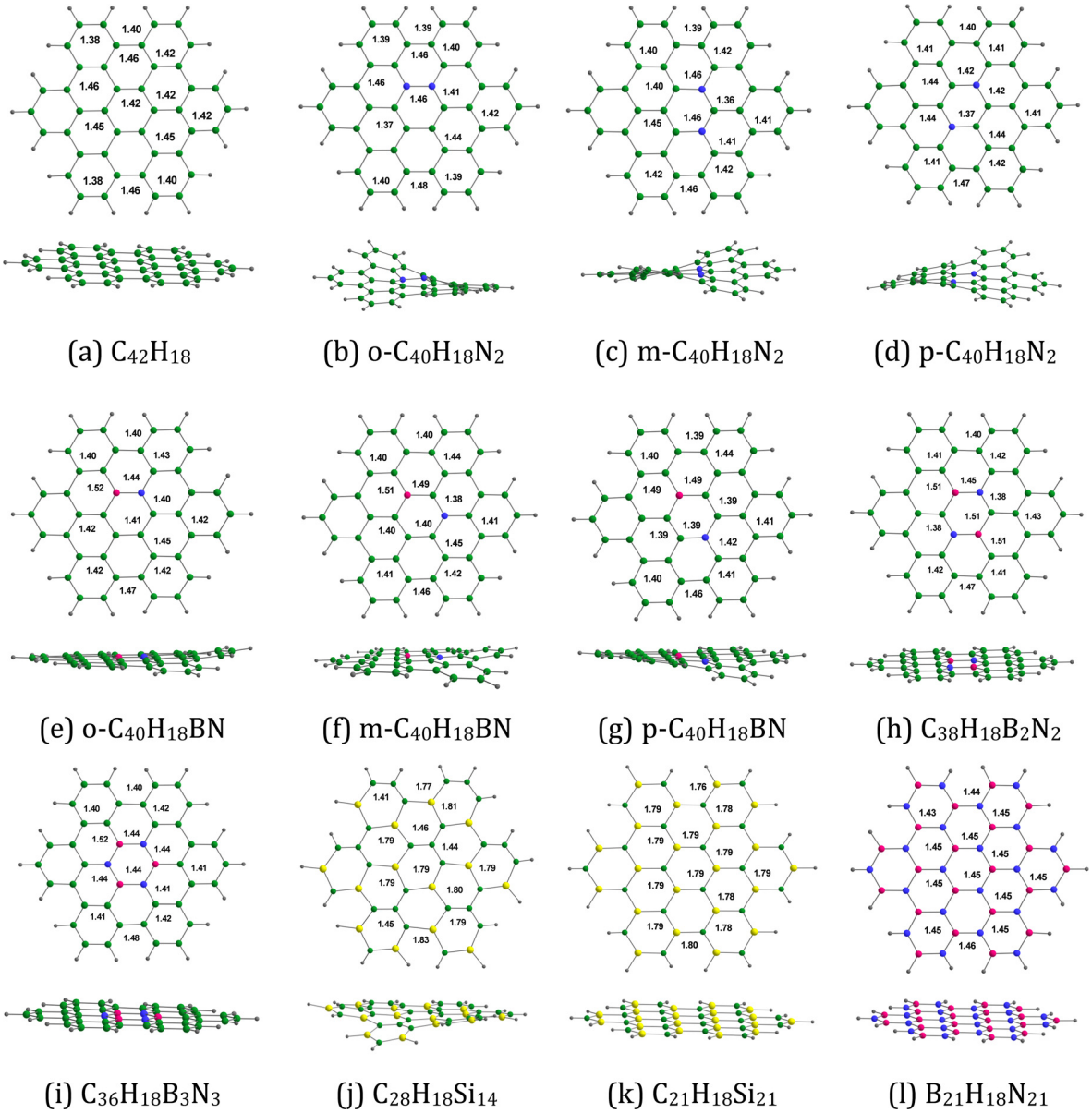

Fig. 2 Optimized structures of (a) $C_{42}H_{18}$, (b) *o*-$C_{40}H_{18}N_2$, (c) *m*-$C_{40}H_{18}N_2$ (d) *p*-$C_{40}H_{18}N_2$, (e) *o*-$C_{40}H_{18}BN$, (f) *m*-$C_{40}H_{18}BN$, (g) *p*-$C_{40}H_{18}BN$, (h) $C_{38}H_{18}B_2N_2$, (i) $C_{36}H_{18}B_3N_3$, (j) $C_{28}H_{18}Si_{14}$, (k) $C_{21}H_{18}Si_{21}$, and (l) $B_{21}H_{18}N_{21}$. The bond distances are given in Å. Color code: green – C, purple – B, blue – N, gray – H, and yellow- – Si.

benzene rings of HBC. This is possibly due to the higher electron-richness of the peripheral benzene rings of HBC as compared to the inner rings of HBC (see the above). These adsorption processes involve the cation–π interactions.[24,41] These interactions are predominantly electrostatic in nature, involving the interaction of Li^+ with the electron cloud of the π-system. Overall, Li^+ is also bound to the peripheral rings of all doped HBC molecules. However, Li^+ is bound to the central ring of *o*-$C_{40}H_{18}N_2$. We observe that Li^+ exhibits a relatively strong adsorption on pristine and doped HBC molecules. For instance, the adsorption distances of Li^+ on these nanoflakes span from 2.20 (Li^+/*m*-$C_{40}H_{18}N_2$ system) to 2.41 Å (Li^+/$C_{21}H_{18}Si_{21}$ system). The adsorption energy data (Table 2) also support this possibility. Here the $E_{ads\text{-}1}$ values were in the range of −67.34 (Li^+/$C_{28}H_{18}Si_{14}$ system) to −47.65 kcal mol^{-1} (Li^+/$B_{21}H_{18}N_{21}$ system). A higher negative value of $E_{ads\text{-}1}$ typically implies a stronger interaction between Li^+ and the nanoflake. The $E_{ads\text{-}1}$ value of the Li^+/HBC system was −51.57 kcal mol^{-1}. This value is more negative than that of the Li^+/$C_{36}H_{18}B_3N_3$ and Li^+/$B_{21}H_{18}N_{21}$ systems. In the case of Li^+ adsorption on N-doped HBC molecules, the absolute values of $E_{ads\text{-}1}$ followed the order *o*-$C_{40}H_{18}N_2$ < *p*-$C_{40}H_{18}N_2$ < *m*-$C_{40}H_{18}N_2$. In the case of Li^+ adsorption on BN-doped HBC molecules, the absolute values of $E_{ads\text{-}1}$ followed the order $B_{21}H_{18}N_{21}$ < $C_{36}H_{18}B_3N_3$ < *o*-$C_{40}H_{18}BN$ < $C_{38}H_{18}B_2N_2$ < *p*-$C_{40}H_{18}BN$ < *m*-$C_{40}H_{18}BN$. The $E_{ads\text{-}1}$ value of the Li^+/$C_{21}H_{18}Si_{21}$

Table 1 V_{min}, E_{HOMO}, E_{LUMO} and $E_{g\text{-}1}$ values of doped HBCs[a]

Nanoflake	V_{min}	E_{HOMO}	E_{LUMO}	$E_{g\text{-}1}$
$C_{42}H_{18}$	−15.56	−6.39	−1.00	5.40
o-$C_{40}H_{18}N_2$	−19.70	−4.89	−1.11	3.78
m-$C_{40}H_{18}N_2$	−24.97	−4.01	−1.55	2.46
p-$C_{40}H_{18}N_2$	−16.44	−4.74	−0.95	3.80
o-$C_{40}H_{18}BN$	−18.64	−6.09	−1.22	4.87
m-$C_{40}H_{18}BN$	−23.41	−5.90	−1.41	4.49
p-$C_{40}H_{18}BN$	−22.53	−6.37	−0.99	5.38
$C_{38}H_{18}B_2N_2$	−18.14	−5.45	−1.74	3.71
$C_{36}H_{18}B_3N_3$	−16.32	−6.73	−0.69	6.05
$C_{28}H_{18}Si_{14}$	−31.38	−5.71	−1.71	4.00
$C_{21}H_{18}Si_{21}$	−28.43	−6.44	−1.14	5.30
$B_{21}H_{18}N_{21}$	−17.57	−8.10	0.89	9.00

[a] The values are given in eV and V_{min} in kcal mol^{-1}.

system (−60.82 kcal mol^{-1}) was less negative than that of the $Li^+/C_{28}H_{18}Si_{14}$ system. Notably, a linear relationship between $E_{ads\text{-}1}$ and MESP V_{min} values of the nanoflakes exists with a correlation coefficient of 0.913 (Fig. 5a). This finding reflects the weaker interactions of Li^+ with the nanoflakes as the MESP V_{min} values of the nanoflakes become less negative. For all cases, the adsorption free energies were negative, indicating the spontaneous nature of the adsorption process (see Table 2). Here the $G_{ads\text{-}1}$ values were in the range of −58.02 ($Li^+/C_{28}H_{18}Si_{14}$ system) to −37.15 kcal mol^{-1} ($Li^+/B_{21}H_{18}N_{21}$ system).

The electron donation from the nanoflakes to Li^+ can be assessed by determining the MESP at the nucleus of Li^+ before and after adsorption. Therefore, $\Delta V_{MESP\text{-}1}$ is calculated by subtracting the MESP at the nucleus of free Li^+ (−5.36 a.u.) from that of Li^+ in the Li^+/nanoflake system. For all cases, the $\Delta V_{MESP\text{-}1}$ values were negative, indicating the electron donation from the nanoflakes to Li^+ (see Table 2). Here the $\Delta V_{MESP\text{-}1}$ values are in the range of −148.34 ($Li^+/C_{21}H_{18}Si_{21}$ system) to −112.35 kcal mol^{-1} ($Li^+/C_{36}H_{18}B_3N_3$ system). The $\Delta V_{MESP\text{-}1}$ value of the Li^+/HBC system is −114.15 kcal mol^{-1}. This value is more negative than that of the $Li^+/C_{36}H_{18}B_3N_3$ system. A linear relationship between $E_{ads\text{-}1}$ and $\Delta V_{MESP\text{-}1}$ values exists with a correlation coefficient of 0.863 (Fig. 5b). This finding reflects that stronger interactions of Li^+ with the nanoflakes push more electron density toward Li^+.

Table 2 also lists the E_{HOMO}, E_{LUMO}, and $E_{g\text{-}2}$ values of the Li^+-adsorbed nanoflakes. Here the E_{HOMO}, E_{LUMO}, and $E_{g\text{-}2}$ values are in the ranges of −10.45 ($Li^+/B_{21}H_{18}N_{21}$ system) to −8.24 eV ($Li^+/C_{38}H_{18}B_2N_2$ system), −4.62 ($Li^+/C_{38}H_{18}B_2N_2$ system) to −3.76 eV ($Li^+/C_{21}H_{18}Si_{21}$ system), and 2.81 (Li^+/*m*-$C_{40}H_{18}N_2$ system) to 6.35 eV ($Li^+/B_{21}H_{18}N_{21}$ system), respectively. The E_{HOMO}, E_{LUMO}, and $E_{g\text{-}2}$ values of the Li^+/HBC system are −8.98, −4.54, and 4.44 eV, respectively. The E_{HOMO} and E_{LUMO} values of all the Li^+-adsorbed nanoflakes are lower than those of the corresponding Li^+-free nanoflakes. In general,

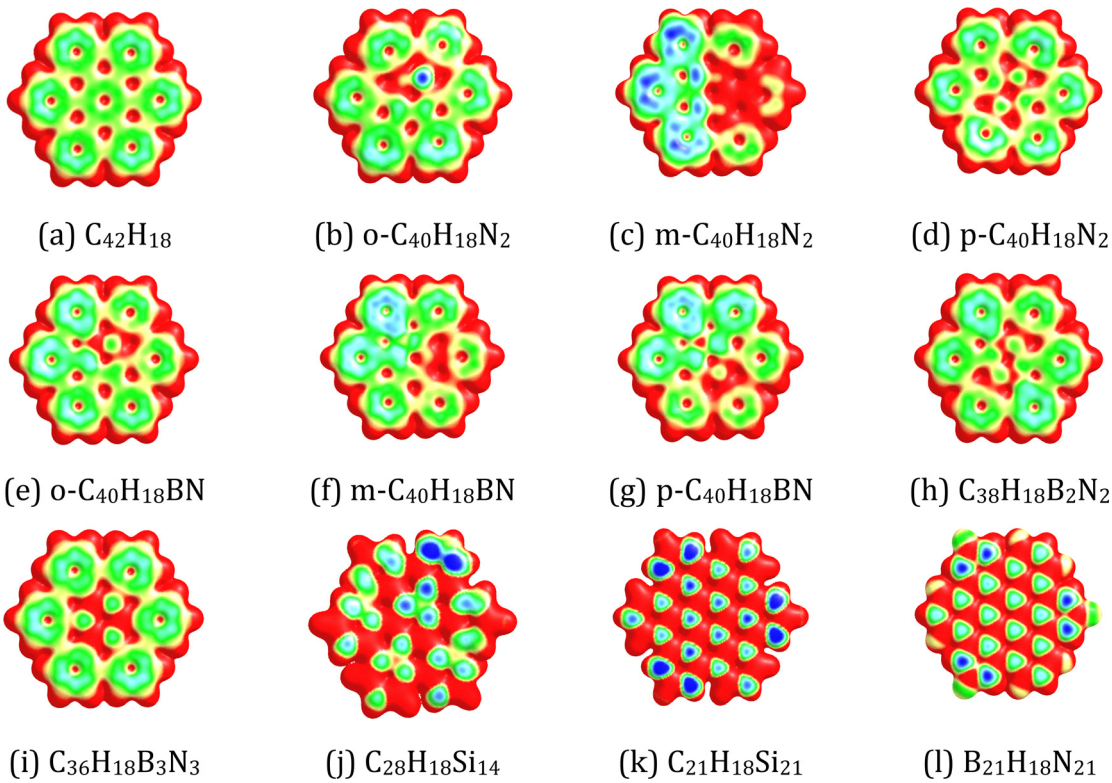

Fig. 3 MESP mapped on the 0.01 a.u. electron density isosurface of (a) $C_{42}H_{18}$, (b) *o*-$C_{40}H_{18}N_2$, (c) *m*-$C_{40}H_{18}N_2$ (d) *p*-$C_{40}H_{18}N_2$, (e) *o*-$C_{40}H_{18}BN$, (f) *m*-$C_{40}H_{18}BN$, (g) *p*-$C_{40}H_{18}BN$, (h) $C_{38}H_{18}B_2N_2$, (i) $C_{36}H_{18}B_3N_3$, (j) $C_{28}H_{18}Si_{14}$, (k) $C_{21}H_{18}Si_{21}$, and (l) $B_{21}H_{18}N_{21}$. The colour coding from blue to red indicates MESP values in the range −0.03 to 0.03 a.u. The colours at the blue end of the spectrum indicate the electron-rich regions, while those toward the red indicate the electron-deficient regions.

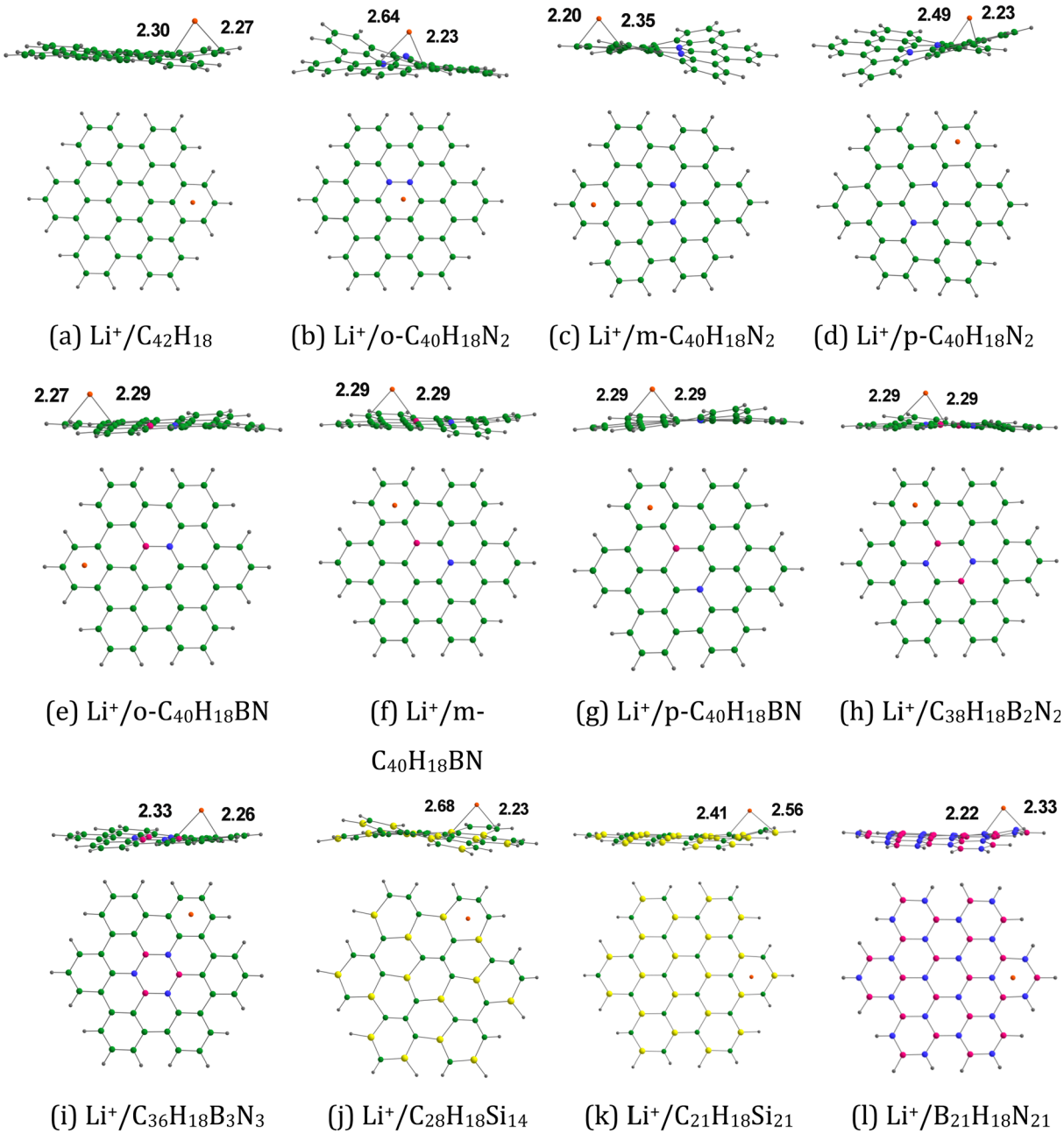

Fig. 4 Optimized structures of Li^+ adsorbed on (a) $C_{42}H_{18}$, (b) *o*-$C_{40}H_{18}N_2$, (c) *m*-$C_{40}H_{18}N_2$ (d) *p*-$C_{40}H_{18}N_2$, (e) *o*-$C_{40}H_{18}BN$, (f) *m*-$C_{40}H_{18}BN$, (g) *p*-$C_{40}H_{18}BN$, (h) $C_{38}H_{18}B_2N_2$, (i) $C_{36}H_{18}B_3N_3$, (j) $C_{28}H_{18}Si_{14}$, (k) $C_{21}H_{18}Si_{21}$, and (l) $B_{21}H_{18}N_{21}$. The bond distances are given in Å. The color code is the same as in Fig. 2. In addition, Li is denoted by the orange color.

a similar trend was obtained for $E_{g\text{-}2}$. The HOMO–LUMO gap decreased by 17.69% due to Li^+ adsorption on HBC (see the $\Delta E_{g\text{-}1}$ values in Table 2). The maximum decrease in the HOMO–LUMO gap is obtained for Li^+ adsorption on $B_{21}H_{18}N_{21}$ (29.45%). The maximum increase in the HOMO–LUMO gap is obtained for Li^+ adsorption on *m*-$C_{40}H_{18}N_2$ (14.03%).

3.1.4. Li adsorption on doped HBC molecules. Fig. 6 provides the optimized configurations and the adsorption distances for the adsorption of Li on pristine and doped HBC molecules. Li is mostly bound to the peripheral rings of these nanoflakes, as observed in the case of Li^+. The adsorption distances of Li on these nanoflakes span from 2.15 (Li/*p*-$C_{40}H_{18}N_2$ system) to 2.25 Å (Li/$C_{38}H_{18}B_2N_2$ system). For these nanoflakes, the adsorption distances of Li^+ (see Fig. 4) are typically larger than those of Li. For instance, the adsorption distances of Li^+ and Li on HBC are 2.27 and 2.17 Å, respectively. However, Li^+ was strongly adsorbed on these nanoflakes in comparison with Li. The adsorption energy data (see Tables 2 and 3) support this possibility. Here, the $E_{ads\text{-}2}$ values are in the range of −33.94 (Li/$C_{38}H_{18}B_2N_2$ system) to −3.93 kcal mol^{-1} (Li/$B_{21}H_{18}N_{21}$ system). The $E_{ads\text{-}2}$ value of the Li/HBC system is −17.39 kcal mol^{-1}. This value is more negative than those of

Table 2 $E_{ads\text{-}1}$, $\Delta V_{MESP\text{-}1}$, E_{HOMO} E_{LUMO}, $E_{g\text{-}2}$ and $\Delta E_{g\text{-}1}$ values of Li^+ adsorbed HBCs[a]

Nanoflake	$E_{ads\text{-}1}$	$G_{ads\text{-}1}$	$\Delta V_{MESP\text{-}1}$	E_{HOMO}	E_{LUMO}	$E_{g\text{-}2}$	$\Delta E_{g\text{-}1}$
$C_{42}H_{18}$	−51.57	−46.58	−114.15	−8.98	−4.54	4.44	−17.69
o-$C_{40}H_{18}N_2$	−52.54	−43.76	−122.27	−8.67	−4.41	4.26	12.73
m-$C_{40}H_{18}N_2$	−63.17	−52.97	−133.74	−7.06	−4.25	2.81	14.03
p-$C_{40}H_{18}N_2$	−52.75	−43.65	−119.68	−7.65	−4.20	3.45	−9.10
o-$C_{40}H_{18}BN$	−55.25	−45.65	−119.46	−8.80	−4.30	4.50	−7.65
m-$C_{40}H_{18}BN$	−59.30	−49.77	−124.32	−8.67	−4.37	4.31	−4.12
p-$C_{40}H_{18}BN$	−58.67	−49.26	−123.26	−9.05	−4.07	4.98	−7.53
$C_{38}H_{18}B_2N_2$	−55.60	−47.70	−121.48	−8.24	−4.62	3.62	−2.49
$C_{36}H_{18}B_3N_3$	−50.81	−45.48	−112.35	−9.05	−4.26	4.79	−20.83
$C_{28}H_{18}Si_{14}$	−67.34	−58.02	−146.76	−8.30	−4.15	4.15	3.81
$C_{21}H_{18}Si_{21}$	−60.82	−51.17	−148.34	−8.40	−3.76	4.64	−12.42
$B_{21}H_{18}N_{21}$	−47.65	−37.15	−114.78	−10.45	−4.11	6.35	−29.45

[a] The values of $E_{ads\text{-}1}$, $G_{ads\text{-}1}$ and $\Delta V_{MESP\text{-}1}$ in kcal mol^{-1}; E_{HOMO}, E_{LUMO}, and $E_{g\text{-}2}$ in eV; $\Delta E_{g\text{-}1}$ in %.

the $Li/C_{36}H_{18}B_3N_3$ and $Li/B_{21}H_{18}N_{21}$ systems. In the case of Li adsorption on N-doped HBC molecules, the absolute values of $E_{ads\text{-}2}$ followed the order *p*-$C_{40}H_{18}N_2$ < *o*-$C_{40}H_{18}N_2$ < *m*-$C_{40}H_{18}N_2$. In the case of Li adsorption on BN-doped HBC molecules, the absolute values of $E_{ads\text{-}2}$ followed the order $B_{21}H_{18}N_{21}$ < $C_{36}H_{18}B_3N_3$ < *p*-$C_{40}H_{18}BN$ < *o*-$C_{40}H_{18}BN$ < *m*-$C_{40}H_{18}BN$ < $C_{38}H_{18}B_2N_2$. The $E_{ads\text{-}2}$ value of the $Li/C_{21}H_{18}Si_{21}$ system (−30.84 kcal mol^{-1}) was less negative than that of the $Li/C_{28}H_{18}Si_{14}$ system (−32.42 kcal mol^{-1}). Here, $E_{ads\text{-}2}$ is not well correlated with the MESP V_{min} values of the nanoflakes (Fig. S2, ESI†). Overall, the adsorption free energies were negative, indicating the spontaneous nature of the adsorption process (see Table 3). However, the $G_{ads\text{-}2}$ value of the $Li/B_{21}H_{18}N_{21}$ system is positive (3.87 kcal mol^{-1}), suggesting that the adsorption of Li on $B_{21}H_{18}N_{21}$ is not spontaneous. $\Delta V_{MESP\text{-}2}$ is calculated by subtracting the MESP at the nucleus of free Li (−5.72 a.u.) from that of Li in the Li/nanoflake system. Overall, the $\Delta V_{MESP\text{-}2}$ values were positive, indicating the electron density transfer from Li to the nanoflakes (see Table 3). However, the $\Delta V_{MESP\text{-}2}$ values were negative for Li adsorption on $C_{21}H_{18}Si_{21}$ and $B_{21}H_{18}N_{21}$. Unlike $E_{ads\text{-}1}$, $E_{ads\text{-}2}$ did not display a correlation with $\Delta V_{MESP\text{-}2}$ (see Fig. S2, ESI†).

Table 3 also lists the E_{HOMO}, E_{LUMO}, and $E_{g\text{-}3}$ values of the Li-adsorbed nanoflakes. Here the E_{HOMO}, E_{LUMO}, and $E_{g\text{-}3}$ values are in the ranges of −4.71 ($Li/C_{21}H_{18}Si_{21}$ system) to −3.10 eV ($Li/B_{21}H_{18}N_{21}$ system), −0.63 ($Li/C_{38}H_{18}B_2N_2$ system) to 0.32 eV ($Li/B_{21}H_{18}N_{21}$ system), and 2.27 (Li/*p*-$C_{40}H_{18}BN$ system) to 3.76 eV ($Li/C_{38}H_{18}B_2N_2$ system), respectively. The E_{HOMO}, E_{LUMO}, and $E_{g\text{-}3}$ values of the Li/HBC system are −3.59, −0.98, and 2.62 eV, respectively. The E_{HOMO} values of all the Li-adsorbed nanoflakes are higher than those of the corresponding Li-free nanoflakes. In general, a similar trend was obtained for $E_{g\text{-}3}$. For all nanoflakes, the E_{LUMO} was not much influenced by the presence of Li. The HOMO–LUMO gap decreased by 51.51% due to Li adsorption on HBC (see $\Delta E_{g\text{-}2}$ values in Table 3). The maximum decrease in the HOMO–LUMO gap is obtained for Li adsorption on $B_{21}H_{18}N_{21}$ (61.99%). However, $E_{g\text{-}1}$ was lower than $E_{g\text{-}3}$ for Li adsorption on *m*-$C_{40}H_{18}N_2$ ($\Delta E_{g\text{-}2}$ of 13.26%) and $C_{38}H_{18}B_2N_2$ ($\Delta E_{g\text{-}2}$ of 1.39%).

3.1.5. Cell voltage. The ΔE_{cell} and V_{cell} values of LIBs based on the pristine and doped HBC molecules are provided in Table 3. Here the ΔE_{cell} and V_{cell} values were in the ranges of −43.72 ($B_{21}H_{18}N_{21}$) to −21.66 kcal mol^{-1} ($C_{38}H_{18}B_2N_2$) and 0.94 ($C_{38}H_{18}B_2N_2$) to 1.90 V ($B_{21}H_{18}N_{21}$), respectively. The less negative the ΔE_{cell}, the lower the V_{cell} of the system. Thus, a nanoflake with a strong interaction with Li^+ and a weak interaction with Li might be regarded as a good candidate for the anode material in metal ion batteries. For instance, in the case of $B_{21}H_{18}N_{21}$, a high V_{cell} value of 1.90 V was obtained because of a high $E_{ads\text{-}1}$ value of −47.65 kcal mol^{-1} (see Table 2) and a low $E_{ads\text{-}2}$ value of −3.93 kcal mol^{-1} (see Table 3). In the case of $C_{38}H_{18}B_2N_2$, a low V_{cell} value of 0.94 V was obtained due to the higher contribution from $E_{ads\text{-}2}$ ($E_{ads\text{-}1}$ value of −55.60 kcal mol^{-1} and $E_{ads\text{-}2}$ value of −33.94 kcal mol^{-1}). The ΔE_{cell} and V_{cell} values of HBC were −34.18 kcal mol^{-1} and 1.48 V, respectively. In the case of N-doped HBC molecules, the V_{cell} values followed the order *o*-$C_{40}H_{18}N_2$ < *m*-$C_{40}H_{18}N_2$ < *p*-$C_{40}H_{18}N_2$. In the case of BN-doped HBC molecules, the V_{cell} values followed the order $C_{38}H_{18}B_2N_2$ < *m*-$C_{40}H_{18}BN$ < $C_{36}H_{18}B_3N_3$ < *o*-$C_{40}H_{18}BN$ < *p*-$C_{40}H_{18}BN$ < $B_{21}H_{18}N_{21}$. The V_{cell} value of $C_{21}H_{18}Si_{21}$ (1.30 V) was lower than that of

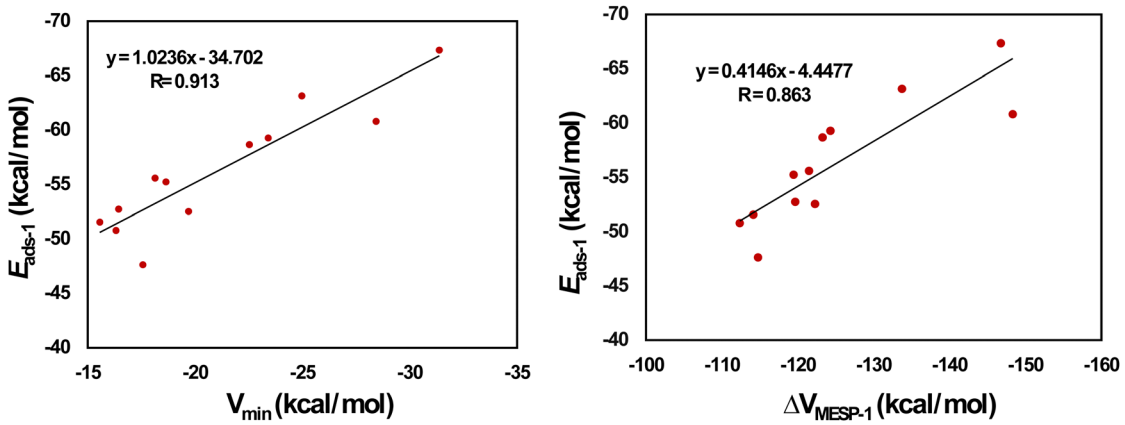

Fig. 5 Correlation between (a) V_{min} and $E_{ads\text{-}1}$ and (b) $\Delta V_{MESP\text{-}1}$ and $E_{ads\text{-}1}$ for Li^+-adsorbed HBCs.

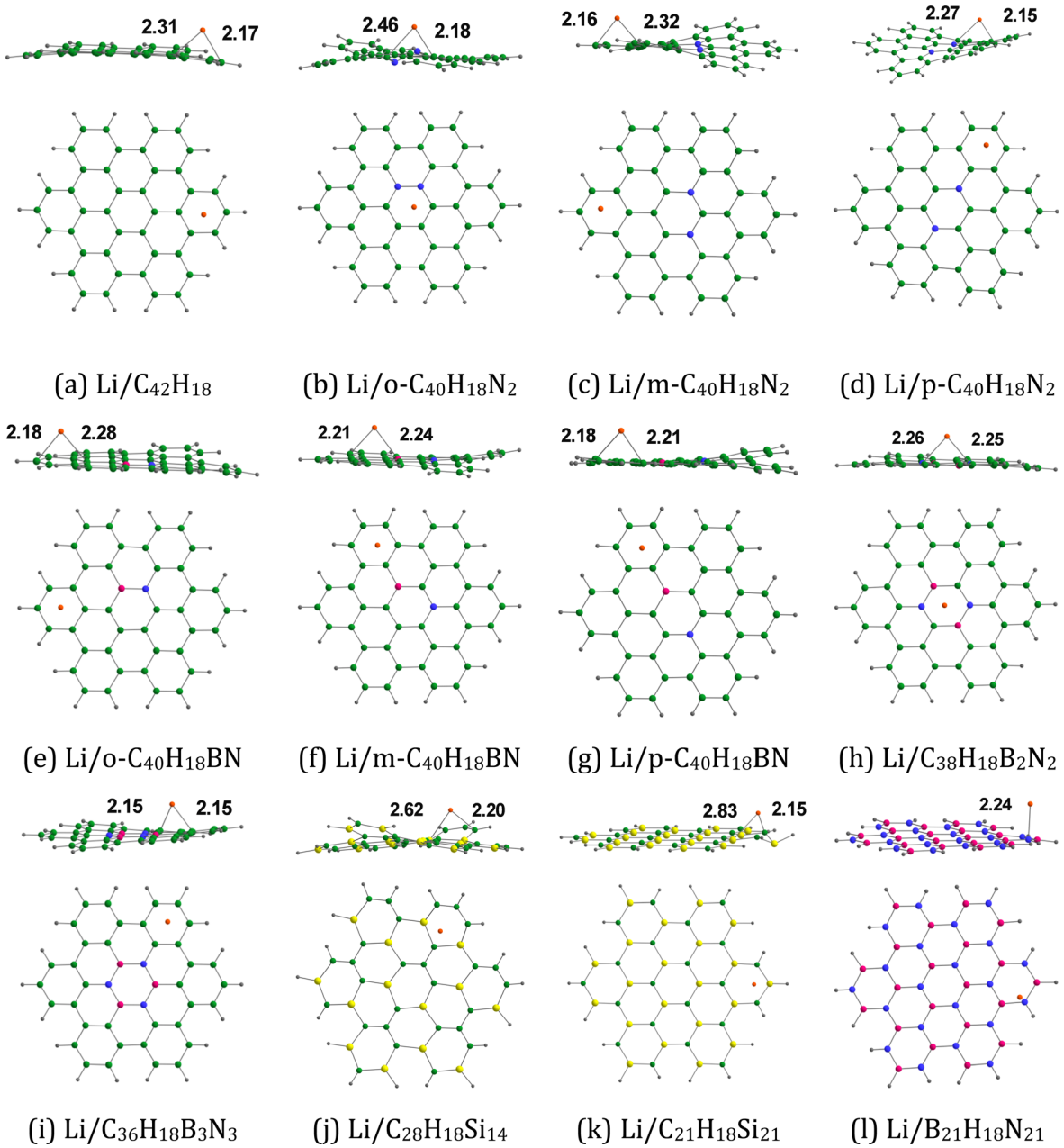

Fig. 6 Optimized structures of Li adsorbed on (a) $C_{42}H_{18}$, (b) *o*-$C_{40}H_{18}N_2$, (c) *m*-$C_{40}H_{18}N_2$ (d) *p*-$C_{40}H_{18}N_2$, (e) *o*-$C_{40}H_{18}BN$, (f) *m*-$C_{40}H_{18}BN$, (g) *p*-$C_{40}H_{18}BN$, (h) $C_{38}H_{18}B_2N_2$, (i) $C_{36}H_{18}B_3N_3$, (j) $C_{28}H_{18}Si_{14}$, (k) $C_{21}H_{18}Si_{21}$, and (l) $B_{21}H_{18}N_{21}$. The bond distances are given in Å. The color code is the same as in Fig. 2. In addition, Li is denoted by the orange color.

$C_{28}H_{18}Si_{14}$ (1.51 V). When considering all the nanoflakes, unlike $E_{ads\text{-}1}$, $E_{ads\text{-}2}$ shows large variations (see Tables 2 and 3). Thus, $E_{ads\text{-}2}$ can have a significant effect on the variation of V_{cell}. A linear relationship between $E_{ads\text{-}2}$ and V_{cell} with a correlation coefficient of 0.765 further supports the significant effect of $E_{ads\text{-}2}$ on the variation of V_{cell} (Fig. S3a, ESI†).

3.2 HBCs and their analogues as anode materials in magnesium-ion batteries

3.2.1. Mg^{2+} adsorption on doped HBC molecules. Fig. 7 provides the optimized configurations and the adsorption distances for the adsorption of Mg^{2+} on pristine and doped HBC molecules. We see that Mg^{2+} is bound to the peripheral benzene rings of HBC, similar to the case of Li^+. Mg^{2+} is also bound to the peripheral rings of all doped HBC molecules except *o*-$C_{40}H_{18}N_2$, *o*-$C_{40}H_{18}N_2$, and *p*-$C_{40}H_{18}N_2$. We find that Mg^{2+} is strongly adsorbed on pristine and doped HBC molecules. For instance, the adsorption distances of Mg^{2+} on these nanoflakes span from 3.69 (Mg^{2+}/*m*-$C_{40}H_{18}N_2$ system) to 2.14 Å (Mg^{2+}/$B_{21}H_{18}N_{21}$ system). The adsorption energy data (Table 4) also support this possibility. Here the $E_{ads\text{-}1}$ values were in the range of −247.44 (Mg^{2+}/*m*-$C_{40}H_{18}N_2$ system) to

Table 3 $E_{ads\text{-}2}$, $\Delta V_{MESP\text{-}2}$, E_{HOMO} E_{LUMO}, $E_{g\text{-}3}$ and $\Delta E_{g\text{-}2}$ values of Li adsorbed HBCs, along with ΔE_{cell} and V_{cell}[a]

Nanoflake	$E_{ads\text{-}2}$	$G_{ads\text{-}2}$	$\Delta V_{MESP\text{-}2}$	E_{HOMO}	E_{LUMO}	$E_{g\text{-}3}$	$\Delta E_{g\text{-}2}$	ΔE_{cell}	V_{cell}
$C_{42}H_{18}$	−17.39	−15.32	16.73	−3.59	−0.98	2.62	−51.51	−34.18	1.48
o-$C_{40}H_{18}N_2$	−23.10	−16.24	14.88	−3.90	−0.88	3.02	−20.22	−29.44	1.28
m-$C_{40}H_{18}N_2$	−30.68	−23.05	20.44	−3.82	−1.04	2.79	13.26	−32.49	1.41
p-$C_{40}H_{18}N_2$	−18.02	−11.74	13.71	−3.64	−0.82	2.82	−25.72	−34.72	1.51
o-$C_{40}H_{18}BN$	−20.81	−13.73	16.42	−3.58	−1.02	2.56	−47.43	−34.44	1.49
m-$C_{40}H_{18}BN$	−26.64	−19.27	18.51	−3.64	−0.97	2.67	−40.52	−32.66	1.42
p-$C_{40}H_{18}BN$	−18.95	−12.63	9.50	−3.35	−1.08	2.27	−57.81	−39.73	1.72
$C_{38}H_{18}B_2N_2$	−33.94	−28.74	21.50	−4.39	−0.63	3.76	1.39	−21.66	0.94
$C_{36}H_{18}B_3N_3$	−16.40	−13.51	13.21	−3.61	−0.84	2.77	−54.25	−34.40	1.49
$C_{28}H_{18}Si_{14}$	−32.42	−25.10	6.07	−3.73	−1.39	2.34	−41.36	−34.92	1.51
$C_{21}H_{18}Si_{21}$	−30.84	−22.75	−18.32	−4.71	−1.15	3.56	−32.85	−29.98	1.30
$B_{21}H_{18}N_{21}$	−3.93	3.87	−25.98	−3.10	0.32	3.42	−61.99	−43.72	1.90

[a] The values of $E_{ads\text{-}2}$, $G_{ads\text{-}2}$, $\Delta V_{MESP\text{-}2}$, and ΔE_{cell} in kcal mol^{-1}; E_{HOMO}, E_{LUMO}, and $E_{g\text{-}3}$ in eV; $\Delta E_{g\text{-}2}$ in %; and V_{cell} in V.

−172.35 kcal mol^{-1} (Mg^{2+}/$B_{21}H_{18}N_{21}$ system). A higher negative value of $E_{ads\text{-}1}$ usually implies a stronger interaction between Mg^{2+} and the nanoflake. The $E_{ads\text{-}1}$ value of the Mg^{2+}/HBC system is −178.09 kcal mol^{-1}. This value is more negative than that of the Mg^{2+}/$C_{36}H_{18}B_3N_3$ and Mg^{2+}/$B_{21}H_{18}N_{21}$ systems. In the case of Mg^{2+} adsorption on N-doped HBC molecules, the absolute values of $E_{ads\text{-}1}$ followed the order *o*-$C_{40}H_{18}N_2$ < *p*-$C_{40}H_{18}N_2$ < *m*-$C_{40}H_{18}N_2$. In the case of Mg^{2+} adsorption on BN-doped HBC molecules, the absolute values of $E_{ads\text{-}1}$ followed the order $B_{21}H_{18}N_{21}$ < $C_{36}H_{18}B_3N_3$ < *o*-$C_{40}H_{18}BN$ < $C_{38}H_{18}B_2N_2$ < *p*-$C_{40}H_{18}BN$ < *m*-$C_{40}H_{18}BN$. The $E_{ads\text{-}1}$ value of the Mg^{2+}/$C_{21}H_{18}Si_{21}$ system (−229.05 kcal mol^{-1}) was less negative than that of the Mg^{2+}/$C_{28}H_{18}Si_{14}$ system (−231.69 kcal mol^{-1}). Here a linear relationship between $E_{ads\text{-}1}$ and MESP V_{min} values of the nanoflakes exists with a correlation coefficient of 0.690 (Fig. 8a). This finding reflects the weaker interactions of Mg^{2+} with the nanoflakes as the MESP V_{min} values of the nanoflakes become less negative. Notably a better correlation was obtained for the adsorption of Li^+ on pristine and doped HBC molecules (see Fig. 5a). For all cases, the adsorption free energies were negative, indicating the spontaneous nature of the adsorption process (see Table 4). Here the $G_{ads\text{-}1}$ values were in the range of −238.37 (Mg^{2+}/*m*-$C_{40}H_{18}N_2$ system) to −161.41 kcal mol^{-1} (Mg^{2+}/$B_{21}H_{18}N_{21}$ system).

$\Delta V_{MESP\text{-}1}$ is calculated here by subtracting the MESP at the nucleus of free Mg^{2+} (−39.11 a.u.) from that of Mg^{2+} in the Mg^{2+}/nanoflake system. For all cases, the $\Delta V_{MESP\text{-}1}$ values were negative, indicating the electron donation from the nanoflakes to Mg^{2+} (see Table 4). Here the $\Delta V_{MESP\text{-}1}$ values are in the range of −387.90 (Mg^{2+}/*m*-$C_{40}H_{18}N_2$ system) to −225.22 kcal mol^{-1} (Mg^{2+}/$C_{36}H_{18}B_3N_3$ system). The $\Delta V_{MESP\text{-}1}$ value of the Mg^{2+}/HBC system was −232.55 kcal mol^{-1}. This value is more negative than those of the Mg^{2+}/$C_{36}H_{18}B_3N_3$ and Mg^{2+}/$B_{21}H_{18}N_{21}$ systems. A linear relationship between $E_{ads\text{-}1}$ and $\Delta V_{MESP\text{-}1}$ values exists with a correlation coefficient of 0.829 (Fig. 8b). This finding reflects that stronger interactions of Mg^{2+} with the nanoflakes push more electron density toward Mg^{2+}.

Table 4 also lists the E_{HOMO}, E_{LUMO}, and $E_{g\text{-}2}$ values of the Mg^{2+}-adsorbed nanoflakes. Here the E_{HOMO}, E_{LUMO}, and $E_{g\text{-}2}$ values are in the ranges of −12.62 (Mg^{2+}/$B_{21}H_{18}N_{21}$ system) to −10.31 eV (Mg^{2+}/$C_{21}H_{18}Si_{21}$ system), −10.02 (Mg^{2+}/$B_{21}H_{18}N_{21}$ system) to −8.05 eV (Mg^{2+}/$C_{21}H_{18}Si_{21}$ system), and 1.35 (Mg^{2+}/$C_{36}H_{18}B_3N_3$ system) to 2.62 eV (Mg^{2+}/*p*-$C_{40}H_{18}N_2$ system), respectively. The E_{HOMO}, E_{LUMO}, and $E_{g\text{-}2}$ values of the Mg^{2+}/HBC system are −11.39, −9.74, and 1.65 eV, respectively. The E_{HOMO} and E_{LUMO} values of all the Mg^{2+}-adsorbed nanoflakes are lower than those of the corresponding Mg^{2+}-free nanoflakes. In general, a similar trend was obtained for $E_{g\text{-}2}$. The HOMO–LUMO gap decreased by 69.35% due to Mg^{2+} adsorption on HBC (see $\Delta E_{g\text{-}1}$ values in Table 4). The maximum decrease in the HOMO–LUMO gap is obtained for Mg^{2+} adsorption on $C_{36}H_{18}B_3N_3$ (77.60%). However, $E_{g\text{-}1}$ was lower than $E_{g\text{-}2}$ for Mg^{2+} adsorption on *m*-$C_{40}H_{18}N_2$ ($\Delta E_{g\text{-}1}$ of 5.64%).

3.2.2. Mg adsorption on doped HBC molecules. Fig. 9 provides the optimized configurations and the adsorption distances for the adsorption of Mg on pristine and doped HBC molecules. Mg is mostly bound to the peripheral rings of these nanoflakes, as observed in the case of Mg^{2+}. The adsorption distances of Mg on these nanoflakes span from 3.10 (Mg/$C_{28}H_{18}Si_{14}$ system) to 3.88 Å (Mg/$C_{21}H_{18}Si_{21}$ system). For these nanoflakes, the adsorption distances of Mg^{2+} (see Fig. 7) are typically smaller than those of Mg. For instance, the adsorption distances of Mg^{2+} and Mg on HBC are 2.30 and 3.61 Å, respectively. Mg^{2+} was strongly adsorbed on these nanoflakes in comparison with Mg. The adsorption energy data (see Tables 4 and 5) support this possibility. Here the $E_{ads\text{-}2}$ values were in the range of −5.11 (Mg/$C_{28}H_{18}Si_{14}$ system) to −2.14 kcal mol^{-1} (Mg/$B_{21}H_{18}N_{21}$ system). The $E_{ads\text{-}2}$ value of the Mg/HBC system was −3.17 kcal mol^{-1}. This value is more negative than that of the Mg/$C_{36}H_{18}B_3N_3$ and Mg/$B_{21}H_{18}N_{21}$ systems. In the case of Mg adsorption on N-doped HBC molecules, the absolute values of $E_{ads\text{-}2}$ followed the order *p*-$C_{40}H_{18}N_2$ < *o*-$C_{40}H_{18}N_2$ < *m*-$C_{40}H_{18}N_2$. In the case of Mg adsorption on BN-doped HBC molecules, the absolute values of $E_{ads\text{-}2}$ followed the order $B_{21}H_{18}N_{21}$ < $C_{36}H_{18}B_3N_3$ < *o*-$C_{40}H_{18}BN$ < *p*-$C_{40}H_{18}BN$ < *m*-$C_{40}H_{18}BN$ < $C_{38}H_{18}B_2N_2$. The $E_{ads\text{-}2}$ value of the Mg/$C_{21}H_{18}Si_{21}$ system (−3.58 kcal mol^{-1}) was less negative than that of the Mg/$C_{28}H_{18}Si_{14}$ system. Here $E_{ads\text{-}2}$ is not well correlated with the MESP V_{min} values of the nanoflakes (Fig. S4, ESI†). Overall, the adsorption free energies were positive, suggesting that the adsorption of Mg on nanoflakes is not spontaneous (see Table 5). However, the $G_{ads\text{-}2}$

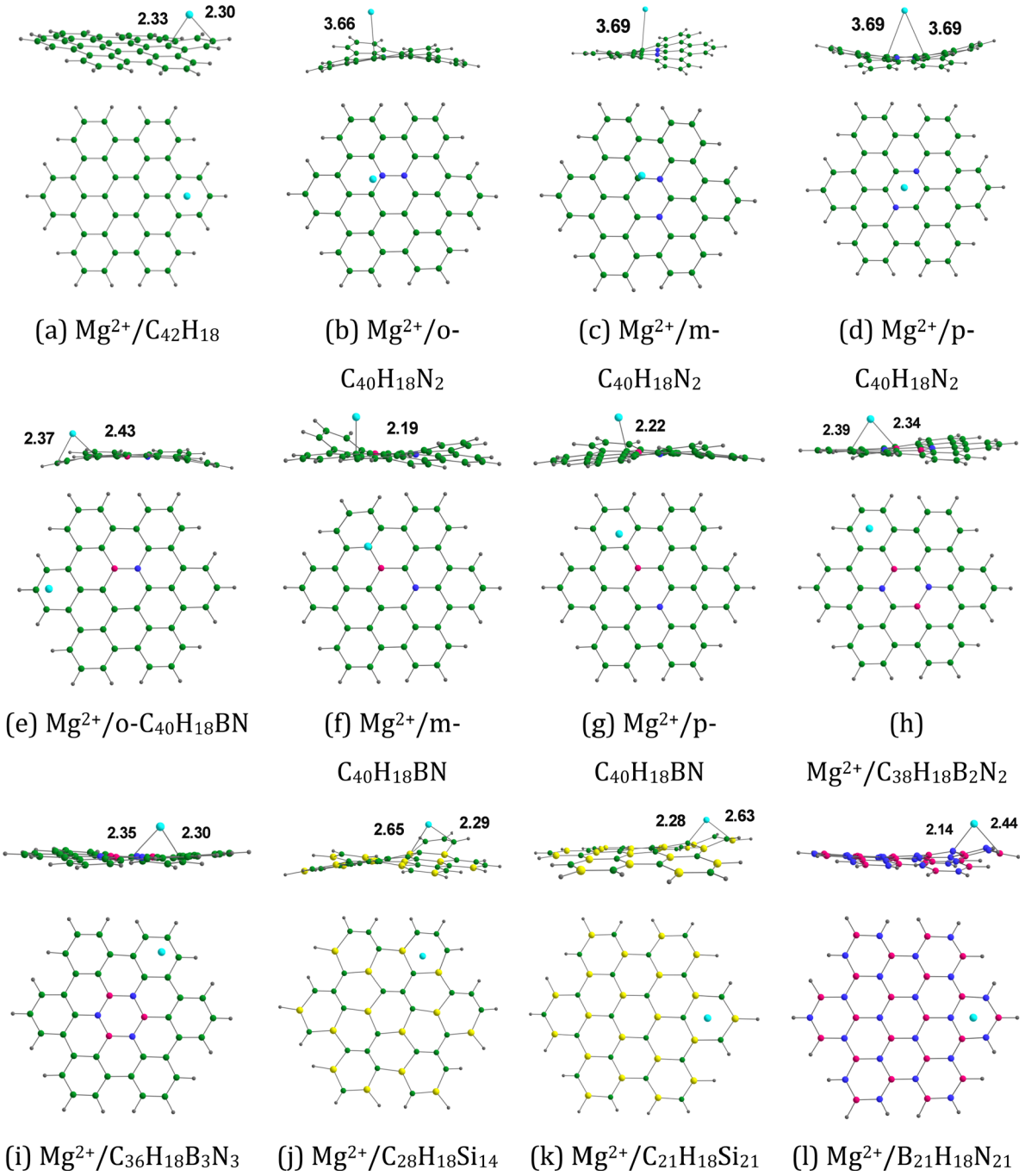

Fig. 7 Optimized structures of Mg^{2+} adsorbed on (a) $C_{42}H_{18}$, (b) *o*-$C_{40}H_{18}N_2$, (c) *m*-$C_{40}H_{18}N_2$ (d) *p*-$C_{40}H_{18}N_2$, (e) *o*-$C_{40}H_{18}BN$, (f) *m*-$C_{40}H_{18}BN$, (g) *p*-$C_{40}H_{18}BN$, (h) $C_{38}H_{18}B_2N_2$, (i) $C_{36}H_{18}B_3N_3$, (j) $C_{28}H_{18}Si_{14}$, (k) $C_{21}H_{18}Si_{21}$, and (l) $B_{21}H_{18}N_{21}$. The bond distances are given in Å. The color code is the same as in Fig. 2. In addition, Mg is denoted by the cyan color.

values of the Mg/$C_{42}H_{18}$ and Mg/$C_{36}H_{18}B_3N_3$ systems are negative, indicating the spontaneous nature of the adsorption process. $\Delta V_{MESP\text{-}2}$ is calculated by subtracting the MESP at the nucleus of free Mg (−39.91 a.u.) from that of Mg in the Mg/nanoflake system. The $\Delta V_{MESP\text{-}2}$ values were negative, indicating the electron donation from the nanoflakes to Mg (see Table 5). Unlike $E_{ads\text{-}1}$, $E_{ads\text{-}2}$ did not display a correlation with $\Delta V_{MESP\text{-}2}$ (see Fig. S4, ESI†).

Table 5 also lists the E_{HOMO}, E_{LUMO}, and $E_{g\text{-}3}$ values of the Mg-adsorbed nanoflakes. Here the E_{HOMO}, E_{LUMO}, and $E_{g\text{-}3}$ values are in the ranges of −5.80 (Mg/$C_{21}H_{18}Si_{21}$ system) to −4.10 eV (Mg/*m*-$C_{40}H_{18}N_2$ system), −1.80 (Mg/$C_{38}H_{18}B_2N_2$ system) to 0.12 eV (Mg/$B_{21}H_{18}N_{21}$ system), and 2.48 (Mg/*m*-$C_{40}H_{18}N_2$ system) to 5.88 eV (Mg/$B_{21}H_{18}N_{21}$ system), respectively. The E_{HOMO}, E_{LUMO}, and $E_{g\text{-}3}$ values of the Mg/HBC system are −5.57, −1.08, and 4.49 eV, respectively. Overall, the E_{HUMO},

Table 4 $E_{ads\text{-}1}$, $\Delta V_{MESP\text{-}1}$, E_{HOMO}, E_{LUMO}, $E_{g\text{-}2}$ and $\Delta E_{g\text{-}1}$ values of Mg^{2+} adsorbed HBCs[a]

Nanoflake	$E_{ads\text{-}1}$	$G_{ads\text{-}1}$	$\Delta V_{MESP\text{-}1}$	E_{HOMO}	E_{LUMO}	$E_{g\text{-}2}$	$\Delta E_{g\text{-}1}$
$C_{42}H_{18}$	−178.09	−173.45	−232.55	−11.39	−9.74	1.65	−69.35
o-$C_{40}H_{18}N_2$	−220.45	−213.17	−382.29	−11.00	−8.62	2.38	−37.05
m-$C_{40}H_{18}N_2$	−247.44	−238.37	−387.90	−10.86	−8.26	2.60	5.64
p-$C_{40}H_{18}N_2$	−220.61	−213.27	−371.99	−11.30	−8.68	2.62	−31.09
o-$C_{40}H_{18}BN$	−187.15	−177.46	−254.82	−11.48	−9.64	1.84	−62.28
m-$C_{40}H_{18}BN$	−196.96	−187.18	−267.51	−11.79	−9.31	2.48	−44.70
p-$C_{40}H_{18}BN$	−192.08	−182.61	−239.19	−11.60	−9.50	2.09	−61.14
$C_{38}H_{18}B_2N_2$	−191.56	−183.82	−282.07	−11.12	−9.29	1.83	−50.62
$C_{36}H_{18}B_3N_3$	−174.18	−168.92	−227.43	−11.32	−9.96	1.35	−77.60
$C_{28}H_{18}Si_{14}$	−231.69	−220.39	−286.89	−10.53	−8.20	2.33	−41.70
$C_{21}H_{18}Si_{21}$	−229.05	−218.53	−294.22	−10.31	−8.05	2.26	−57.34
$B_{21}H_{18}N_{21}$	−172.35	−161.41	−225.22	−12.62	−10.02	2.60	−71.06

[a] The values of $E_{ads\text{-}1}$, $G_{ads\text{-}1}$ and $\Delta V_{MESP\text{-}1}$ in kcal mol^{-1}; E_{HOMO}, E_{LUMO}, and $E_{g\text{-}2}$ in eV; $\Delta E_{g\text{-}1}$ in %.

E_{LUMO} and E_g values of all the nanoflakes are not much influenced by the presence of Mg. The HOMO–LUMO gap decreased by 16.73% due to Mg adsorption on HBC (see $\Delta E_{g\text{-}2}$ values in Table 5). The maximum decrease in the HOMO–LUMO gap is obtained for Mg adsorption on $B_{21}H_{18}N_{21}$ (34.65%).

3.2.3. Cell voltage. The ΔE_{cell} and V_{cell} values of MIBs based on the pristine and doped HBC molecules are provided in Table 5. Here the ΔE_{cell} and V_{cell} values were in the ranges of −243.95 (*m*-$C_{40}H_{18}N_2$) to −170.21 kcal mol^{-1} ($B_{21}H_{18}N_{21}$) and 3.69 ($B_{21}H_{18}N_{21}$) to 5.29 V (*m*-$C_{40}H_{18}N_2$), respectively. As previously noted, a nanoflake with a strong interaction with Mg^{2+} and a weak interaction with Mg might be regarded as a good candidate for the anode material in metal ion batteries. For instance, in the case of *m*-$C_{40}H_{18}N_2$, a high V_{cell} value of 5.29 V was obtained because of a high $E_{ads\text{-}1}$ value of −247.44 kcal mol^{-1} (see Table 4) and a low $E_{ads\text{-}2}$ value of −3.50 kcal mol^{-1} (see Table 5). The ΔE_{cell} and V_{cell} values of HBC were −174.91 kcal mol^{-1} and 3.79 V, respectively. In the case of N-doped HBC molecules, the V_{cell} values followed the order *o*-$C_{40}H_{18}N_2$ < *p*-$C_{40}H_{18}N_2$ < *m*-$C_{40}H_{18}N_2$. In the case of BN-doped HBC molecules, the V_{cell} values followed the order $B_{21}H_{18}N_{21}$ < $C_{36}H_{18}B_3N_3$ < *o*-$C_{40}H_{18}BN$ < $C_{38}H_{18}B_2N_2$ < *p*-$C_{40}H_{18}BN$ < *m*-$C_{40}H_{18}BN$. The V_{cell} value of $C_{21}H_{18}Si_{21}$ (4.89 V) was slightly lower than that of $C_{28}H_{18}Si_{14}$ (4.91 V). When considering all the nanoflakes, unlike $E_{ads\text{-}2}$, $E_{ads\text{-}1}$ shows large variations (see Tables 4 and 5). Thus, here, $E_{ads\text{-}1}$ can have a significant effect on the variation of V_{cell}. A strong linear relationship between $E_{ads\text{-}1}$ and V_{cell} further supports the significant effect of $E_{ads\text{-}1}$ on the variation of V_{cell} (see Fig. S3b, ESI†).

The changes in E_g could influence the electrical conductivity (σ) of the material. The relationship between σ and E_g is given as:[42]

$$\sigma \propto \exp(-E_g/2kT)$$

where k is the Boltzmann constant and T is the temperature. Our results show that the $E_{g\text{-}1}$ values of the doped HBC molecules are lower than those of the pristine HBC. A smaller $E_{g\text{-}1}$ value indicates a higher electronic conductivity. Furthermore, the E_g values of the cation/metal-adsorbed nanoflakes were usually lower than those of the cation/metal-free nanoflakes.

The MESP is a real physical property which can be determined using X-ray diffraction techniques or computational methods. The MESP analyses showed that the replacement of the C atoms of HBC by N/BN/Si units provides a more electron-rich system than the parent HBC molecule. Importantly, we observed stronger interactions of Li^+ and Mg^{2+} with the nanoflakes as the MESP minimum values of the nanoflakes became more negative. We observed weaker interactions of Li^+ and Mg^{2+} with the nanoflakes as the MESP minimum values of the nanoflakes become less negative. The adsorption energy of Li has a significant effect on the variation of V_{cell} of LIBs, while the adsorption energy of Mg^{2+} has a significant effect on the variation of V_{cell} of MIBs. Furthermore, the storage capacity ($C = (n \times z \times F \times 10^3)/M$, where n is the maximum number of adsorbed metal atoms and M is the molecular mass of the electrode) is an important factor for the performance of metal-ion batteries.[23] Such nanoflakes are promising anode materials for high-capacity metal-ion batteries. For example, the lithium storage capacity of coronene was 536.2 mA h g^{-1} and the magnesium storage capacity of HBC was 923.1 mA h g^{-1}.[23,27]

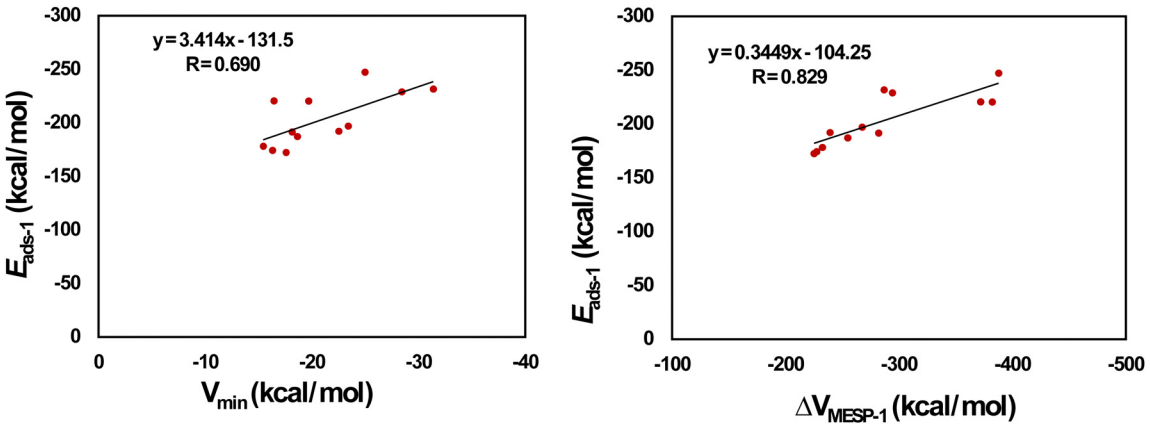

Fig. 8 Correlation between (a) V_{min} and $E_{ads\text{-}1}$ (b) $\Delta V_{MESP\text{-}1}$ and $E_{ads\text{-}1}$ for Mg^{2+}-adsorbed HBCs.

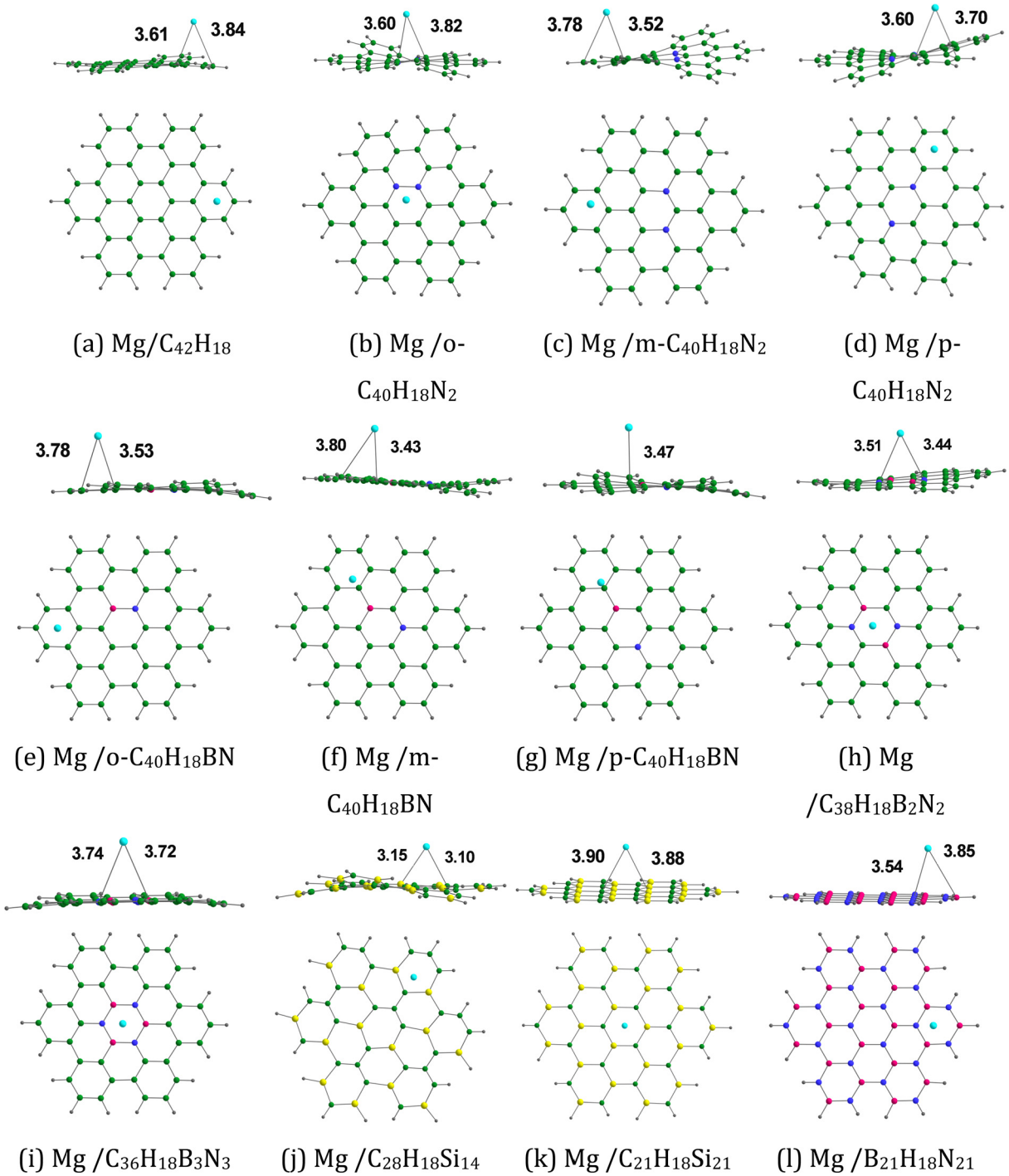

Fig. 9 Optimized structures of Mg adsorbed on (a) $C_{42}H_{18}$, (b) *o*-$C_{40}H_{18}N_2$, (c) *m*-$C_{40}H_{18}N_2$ (d) *p*-$C_{40}H_{18}N_2$, (e) *o*-$C_{40}H_{18}BN$, (f) *m*-$C_{40}H_{18}BN$, (g) *p*-$C_{40}H_{18}BN$, (h) $C_{38}H_{18}B_2N_2$, (i) $C_{36}H_{18}B_3N_3$, (j) $C_{28}H_{18}Si_{14}$, (k) $C_{21}H_{18}Si_{21}$, and (l) $B_{21}H_{18}N_{21}$. The bond distances are given in Å. The color code is the same as in Fig. 2. In addition, Mg is denoted by the cyan color.

For a comparison, the lithium storage capacity of graphite is 372 mA h g^{-1}, that of Sc_2C MXene is 462 mA h g^{-1}, that of graphene-like C_2N is 671.7 mA h g^{-1}, and that of pentagraphyne is 687 mA h g^{-1}.[23] This work could provide insights into the design and exploration of anode materials suitable for metal ion batteries.

The doping process and/or the adsorption process could affect the planar structure of the HBC molecule. The formation of non-planar structures is more evident in *o*-$C_{40}H_{18}N_2$, *m*-$C_{40}H_{18}N_2$, and *p*-$C_{40}H_{18}N_2$ (see Fig. 2) and Mg^{2+}-adsorbed nanoflakes (see Fig. 7). The diffusion of Li^+/Li/Mg^{2+}/Mg on the nanoflake surface could be an important factor for battery applications.[43] For example, the lower diffusion barrier of Li^+ accelerates the charging and discharging process of the battery.[43] We plan to study the diffusion processes in a future publication.

Table 5 $E_{ads\text{-}2}$, $\Delta V_{MESP\text{-}2}$, E_{HOMO} E_{LUMO}, $E_{g\text{-}3}$ and $\Delta E_{g\text{-}2}$ values of Mg adsorbed HBCs, along with ΔE_{cell} and V_{cell}[a]

Nanoflake	$E_{ads\text{-}2}$	$G_{ads\text{-}2}$	$\Delta V_{MESP\text{-}2}$	E_{HOMO}	E_{LUMO}	$E_{g\text{-}3}$	$\Delta E_{g\text{-}2}$	ΔE_{cell}	V_{cell}
$C_{42}H_{18}$	−3.17	−0.65	−12.38	−5.57	−1.08	4.49	−16.73	−174.91	3.79
o-$C_{40}H_{18}N_2$	−3.37	2.21	−12.13	−4.95	−1.18	3.77	−0.29	−217.08	4.71
m-$C_{40}H_{18}N_2$	−3.50	2.56	−18.73	−4.10	−1.62	2.48	0.66	−243.95	5.29
p-$C_{40}H_{18}N_2$	−3.34	2.94	−11.96	−4.83	−1.03	3.80	0.07	−217.27	4.71
o-$C_{40}H_{18}BN$	−3.20	3.03	−14.90	−5.45	−1.31	4.14	−15.01	−183.95	3.99
m-$C_{40}H_{18}BN$	−3.61	2.58	−17.56	−5.30	−1.50	3.80	−15.38	−193.36	4.19
p-$C_{40}H_{18}BN$	−3.48	2.93	−17.12	−5.33	−1.09	4.24	−21.27	−188.60	4.09
$C_{38}H_{18}B_2N_2$	−4.73	0.07	−9.53	−5.54	−1.80	3.74	0.81	−186.83	4.05
$C_{36}H_{18}B_3N_3$	−2.57	−2.06	−7.58	−5.74	−0.71	5.03	−16.82	−171.62	3.72
$C_{28}H_{18}Si_{14}$	−5.11	1.81	−10.95	−5.00	−1.76	3.24	−18.98	−226.58	4.91
$C_{21}H_{18}Si_{21}$	−3.58	1.95	−3.77	−5.80	−1.15	4.65	−12.27	−225.46	4.89
$B_{21}H_{18}N_{21}$	−2.14	3.89	−7.07	−5.76	0.12	5.88	−34.65	−170.21	3.69

[a] The values of $E_{ads\text{-}2}$, $G_{ads\text{-}2}$, $\Delta V_{MESP\text{-}2}$, and ΔE_{cell} in kcal mol^{-1}; E_{HOMO}, E_{LUMO}, and $E_{g\text{-}3}$ in eV; $\Delta E_{g\text{-}2}$ in %; and V_{cell} in V.

4. Conclusions

DFT studies were carried out to understand the adsorption process of Li^+, Li, Mg^{2+}, and Mg on twelve adsorbents (pristine and N/BN/Si-doped HBC molecules $C_{42}H_{18}$, *o*-$C_{40}H_{18}N_2$, *m*-$C_{40}H_{18}N_2$, *p*-$C_{40}H_{18}N_2$, *o*-$C_{40}H_{18}BN$, *m*-$C_{40}H_{18}BN$, *p*-$C_{40}H_{18}BN$, $C_{38}H_{18}B_2N_2$, $C_{36}H_{18}B_3N_3$, $C_{28}H_{18}Si_{14}$, $C_{21}H_{18}Si_{21}$, and $B_{21}H_{18}N_{21}$). The XY (X = C, B; Y = C, N, Si) bond lengths in the pristine and doped HBC molecules span from 1.36 to 1.83 Å. In all cases, the carbon–silicon bond lengths (>1.76 Å) are significantly longer than the carbon–carbon bond lengths. The MESP analyses show that the replacement of C atoms of HBC by N/BN/Si units can provide a more electron-rich system than the parent HBC molecule.

Li^+ exhibits a relatively strong adsorption on pristine and doped HBC molecules. The adsorption distances of Li^+ on these nanoflakes span from 2.20 (*m*-$C_{40}H_{18}N_2$) to 2.41 Å ($C_{21}H_{18}Si_{21}$). Here the $E_{ads\text{-}1}$ values were in the range of −67.34 (Li^+/$C_{28}H_{18}Si_{14}$ system) to −47.65 kcal mol^{-1} (Li^+/$B_{21}H_{18}N_{21}$ system). For the Li/nanoflake system, the $E_{ads\text{-}2}$ values were in the range of −33.94 (Li/$C_{38}H_{18}B_2N_2$ system) to −3.93 kcal mol^{-1} (Li/$B_{21}H_{18}N_{21}$ system). Mg^{2+} also exhibits a relatively strong adsorption on the pristine and doped HBC molecules. Here the $E_{ads\text{-}1}$ values were in the range of −247.44 (Mg^{2+}/*m*-$C_{40}H_{18}N_2$ system) to −172.35 kcal mol^{-1} (Mg^{2+}/$B_{21}H_{18}N_{21}$ system). Our results suggest the weaker interactions of Li^+ and Mg^{2+} with the nanoflakes as the MESP V_{min} values of the nanoflakes become less negative. In all studied systems, we found electron donation from the nanoflakes to Li^+ and Mg^{2+}. For the Mg/nanoflake system, the $E_{ads\text{-}2}$ values were in the range of −5.11 (Mg/$C_{28}H_{18}Si_{14}$ system) to −2.14 kcal mol^{-1} (Mg/$B_{21}H_{18}N_{21}$ system). The HOMO–LUMO gap of the cation/metal-adsorbed nanoflakes was usually lower than that of the cation/metal-free nanoflakes.

A nanoflake with a strong interaction with Li^+/Mg^{2+} and a weak interaction with Li/Mg might be regarded as a good candidate for the anode material in metal ion batteries. Among the studied anode materials for LIBs, the highest V_{cell} value of 1.90 V was obtained for $B_{21}H_{18}N_{21}$ because of the high $E_{ads\text{-}1}$ value of −47.65 kcal mol^{-1} and the low $E_{ads\text{-}2}$ value of −3.93 kcal mol^{-1}. Among the studied anode materials for MIBs, the highest V_{cell} value of 5.29 V was obtained for *m*-$C_{40}H_{18}N_2$ because of the high $E_{ads\text{-}1}$ value of −247.44 kcal mol^{-1} and the low $E_{ads\text{-}2}$ value of −3.50 kcal mol^{-1}. For LIBs, $E_{ads\text{-}2}$ has a significant effect on the variation of V_{cell}, while for MIBs, $E_{ads\text{-}1}$ has a significant effect on the variation of V_{cell}.

Data availability

The data that support the findings of this study are available upon request from the corresponding author.

Conflicts of interest

There are no conflicts to declare.

Acknowledgements

This publication is based upon work supported by the King Abdullah University of Science and Technology (KAUST) Office of Sponsored Research (OSR) under Award No. ORFS-2022-CRG11-5028. R. G. S. N. and A. K. N. N. would like to thank KAUST for providing computational resources of the Shaheen II supercomputer.

References

1 G. E. Blomgren, *J. Electrochem. Soc.*, 2017, **164**, A5019.
2 M. S. Whittingham, *Chem. Rev.*, 2004, **104**, 4271–4302.
3 V. Ruiz, A. Pfrang, A. Kriston, N. Omar, P. Van den Bossche and L. Boon-Brett, *Renewable Sustainable Energy Rev.*, 2018, **81**, 1427–1452.
4 W. Li, M. Li, K. R. Adair, X. Sun and Y. Yu, *J. Mater. Chem. A*, 2017, **5**, 13882–13906.
5 R. Raccichini, A. Varzi, S. Passerini and B. Scrosati, *Nat. Mater.*, 2015, **14**, 271–279.
6 S. Chang, X. Jin, Q. He, T. Liu, J. Fang, Z. Shen, Z. Li, S. Zhang, M. Dahbi, J. Alami, K. Amine, A.-D. Li, H. Zhang and J. Lu, *Nano Lett.*, 2022, **22**, 263–270.

7 J. Park, C. W. Lee, S. H. Joo, J. H. Park, C. Hwang, H.-K. Song, Y. S. Park, S. K. Kwak, S. Ahn and S. J. Kang, *J. Mater. Chem. A*, 2018, **6**, 12589–12597.
8 W. Yuan, Y. Zhang, L. Cheng, H. Wu, L. Zheng and D. Zhao, *J. Mater. Chem. A*, 2016, **4**, 8932–8951.
9 A. Arya, S.-L. Hsu, C.-Y. Liu, M.-Y. Chang, J.-K. Chang, E. Y.-T. Li and Y.-S. Su, *Small Struct.*, 2024, 2400273.
10 L. G. Bulusheva, A. V. Okotrub, A. G. Kurenya, H. Zhang, H. Zhang, X. Chen and H. Song, *Carbon*, 2011, **49**, 4013–4023.
11 L. Zhang, G. Xia, Z. Guo, X. Li, D. Sun and X. Yu, *Int. J. Hydrogen Energy*, 2016, **41**, 14252–14260.
12 Z.-S. Wu, W. Ren, L. Xu, F. Li and H.-M. Cheng, *ACS Nano*, 2011, **5**, 5463–5471.
13 H. Yue, F. Li, Z. Yang, J. Tang, X. Li and D. He, *Mater. Lett.*, 2014, **120**, 39–42.
14 G. Li, B. Huang, Z. Pan, X. Su, Z. Shao and L. An, *Energy Environ. Sci.*, 2019, **12**, 2030–2053.
15 J. A. Blázquez, R. R. Maça, O. Leonet, E. Azaceta, A. Mukherjee, Z. Zhao-Karger, Z. Li, A. Kovalevsky, A. Fernández-Barquín and A. R. Mainar, *Energy Environ. Sci.*, 2023, **16**, 1964–1981.
16 V. S. Thakur and S. Banerjee, *J. Phys. Chem. C*, 2024, **128**, 7865–7875.
17 M. Krieg, F. Reicherter, P. Haiss, M. Ströbele, K. Eichele, M.-J. Treanor, R. Schaub and H. F. Bettinger, *Angew. Chem., Int. Ed.*, 2015, **54**, 8284–8286.
18 X.-Y. Wang, X. Yao, A. Narita and K. Müllen, *Acc. Chem. Res.*, 2019, **52**, 2491–2505.
19 A. Hosseinian, A. Bekhradnia, E. Vessally, L. Edjlali and M. D. Esrafili, *J. Mol. Graphics Modell.*, 2017, **73**, 101–107.
20 W. Zhang, G. Liu, J. Cao, Y. Chen, L. Gao, G. Liu, G. Dai and Q. Wang, *Chem. – Asian J.*, 2022, **17**, e202200340.
21 D. Wang and J. Zhao, *Comput. Theor. Chem.*, 2020, **1185**, 112880.
22 A. Hosseinian, E. Vessally, M. Babazadeh, L. Edjlali and M. Es'haghi, *J. Phys. Chem. Solids*, 2018, **115**, 277–282.
23 R. Geetha Sadasivan Nair, A. K. Narayanan Nair and S. Sun, *Sci. Rep.*, 2024, **14**, 15220.
24 P. K. Ramya and C. H. Suresh, *J. Phys. Chem. A*, 2023, **127**, 2511–2522.
25 X. Wu, Z. Zhang and H. Soleymanabadi, *Solid State Commun.*, 2020, **306**, 113770.
26 R. Rahimi and M. Solimannejad, *J. Mol. Model.*, 2020, **26**, 157.
27 A. Hassanpour, N. Farhami, M. Derakhshande, P. Delir Kheirollahi Nezhad, A. Ebadi and S. Ebrahimiasl, *Inorg. Chem. Commun.*, 2021, **129**, 108656.
28 A. A. Peyghan and J. Beheshtian, *Thin Solid Films*, 2020, **704**, 137979.
29 L. Buenaño, Y. Ajaj, C. Padilla, B. Vaca Barahona, N. Mejía, R. B. D. Real, B. S. R. Oviedo, J. J. F. Fiallos and S. K. Saraswat, *Chem. Phys.*, 2024, **579**, 112194.
30 C. H. Suresh, G. S. Remya and P. K. Anjalikrishna, *Wiley Interdiscip. Rev.:Comput. Mol. Sci.*, 2022, **12**, e1601.
31 G. S. Remya and C. H. Suresh, *New J. Chem.*, 2018, **42**, 3602–3608.
32 G. S. Remya and C. H. Suresh, *New J. Chem.*, 2019, **43**, 14634–14642.
33 M. J. Frisch, G. W. Trucks, H. B. Schlegel, G. E. Scuseria, M. A. Robb, J. R. Cheeseman, G. Scalmani, V. Barone and G. A. Petersson, *et al.*, *Gaussian 16, Rev.B.01*, Gaussian, Inc., Wallingford, CT, 2016.
34 Y. Zhao and D. G. Truhlar, *Theor. Chem. Acc.*, 2008, **120**, 215–241.
35 S. F. Boys and F. Bernardi, *Mol. Phys.*, 1970, **19**, 553–566.
36 Y.-X. Yu, *J. Phys. Chem. C*, 2016, **120**, 5288–5296.
37 R. Goddard, M. W. Haenel, W. C. Herndon, C. Krueger and M. Zander, *J. Am. Chem. Soc.*, 1995, **117**, 30–41.
38 E. Vessally, S. Soleimani-Amiri, A. Hosseinian, L. Edjlali and A. Bekhradnia, *Appl. Surf. Sci.*, 2017, **396**, 740–745.
39 F. Mittendorfer and J. Hafner, *Surf. Sci.*, 2001, **472**, 133–153.
40 A. E. Kuznetsov, *Comput. Theor. Chem.*, 2020, **1188**, 112973.
41 F. B. Sayyed and C. H. Suresh, *J. Phys. Chem. A*, 2011, **115**, 9300–9307.
42 Z. A. Alothman, M. M. Alam, M. Naushad and R. Bushra, *Int. J. Electrochem. Sci.*, 2015, **10**, 2663–2684.
43 M. Weiss, R. Ruess, J. Kasnatscheew, Y. Levartovsky, N. R. Levy, P. Minnmann, L. Stolz, T. Waldmann, M. Wohlfahrt-Mehrens, D. Aurbach, M. Winter, Y. Ein-Eli and J. Janek, *Adv. Energy Mater.*, 2021, **11**, 2101126.